Bi-allelic loss of function variants in *COX20* gene cause autosomal recessive sensory neuronopathy

Hai-Lin Dong,[1] Yin Ma,[1] Hao Yu,[1] Qiao Wei,[1] Jia-Qi Li,[1] Gong-Lu Liu,[1] Hong-Fu Li,[1] Lei Chen,[1,2] Dian-Fu Chen,[1,2] Ge Bai[1,2,3] and Zhi-Ying Wu[1,2,3,4]

Abstract

Sensory neuronopathies are a rare and distinct subgroup of peripheral neuropathies, characterized by degeneration of the dorsal root ganglia neurons. About 50% of sensory neuronopathies are idiopathic and genetic causes remain to be clarified. Through a combination of homozygosity mapping and whole exome sequencing, we linked an autosomal recessive sensory neuronopathy to pathogenic variants in *COX20* gene. We identified 8 unrelated families from the eastern China population carrying a founder variant c.41A>G (p. Lys14Arg) within *COX20* in either a homozygous or compound heterozygous state. All patients displayed sensory ataxia with non-length-dependent sensory potentials decrease. *COX20* encodes a key transmembrane protein implicated in the assembly of mitochondrial complex IV. We showed that *COX20* variants lead to reduction of COX20 protein in patient's fibroblasts and transfected cell lines, consistent with a loss-of-function mechanism. Knockdown of *COX20* expression in ND7/23 sensory neuron cells resulted in complex IV deficiency and perturbed assembly of complex IV, which subsequently compromised cell spare respiratory capacity and reduced cell proliferation under metabolic stress. Consistent with mitochondrial dysfunction in knockdown cells, reduced complex IV assembly, enzyme activity and oxygen consumption rate were also found in patients' fibroblasts. We speculated that the mechanism of *COX20* was similar to other causative genes (e.g. *SURF1*, *COX6A1*, *COA3* and *SCO2*) for peripheral neuropathies, all of which were functionally important in the structure and assembly of complex IV. Our study identifies a novel causative gene for the autosomal recessive sensory neuronopathy, whose

vital function in complex IV and high expression in the proprioceptive sensory neuron further underlines loss of COX20 contributing to mitochondrial bioenergetic dysfunction as a mechanism in peripheral sensory neuron disease.

Author affiliations:

1 Department of Neurology and Research Center of Neurology in Second Affiliated Hospital, Hangzhou, China

2 Key Laboratory of Medical Neurobiology of Zhejiang Province, Zhejiang University School of Medicine, Hangzhou, China

3 NHC and CAMS Key Laboratory of Medical Neurobiology, MOE Frontier Science Center for Brain Research and Brain-Machine Integration, School of Brain Science and Brain Medicine, Zhejiang University, Hangzhou, China

4 CAS Center for Excellence in Brain Science and Intelligence Technology, Shanghai, China

Correspondence to: Zhi-Ying Wu, MD, PhD

Department of Neurology and Research Center of Neurology in Second Affiliated Hospital, and Key Laboratory of Medical Neurobiology of Zhejiang Province, Zhejiang University School of Medicine, 88 Jiefang Road, Hangzhou, 310009, China

E-mail: zhiyingwu@zju.edu.cn

Keywords: sensory neuronopathy; *COX20* gene; complex IV deficiency; loss of function

Introduction

Sensory neuronopathies, also called sensory neuron disease or ganglionopathy, are a rare and distinct subgroup of clinically and genetically heterogeneous peripheral neuropathies, whose symptoms vary and depend on the type of primary sensory neurons involved in the dorsal root ganglion (Sghirlanzoni *et al.*, 2005). Damage to small-dark cells with unmyelinated (C) nerve fibers results in superficial sensory loss or neuropathic pain. While damage to large-light cells with heavily and moderately myelinated A fibers (Aα and Aβ, respectively) results in abnormal proprioception, depressed or absent reflexes and sensory ataxia (Gwathmey and Pearson, 2019). Sensory neuronopathies are commonly caused by various acquired pathologies, including paraneoplastic disease, immune-mediated disease, toxic causes, infections, etc (Damasceno *et al.*, 2008). Sensory neuronopathies also occur in several genetic and degenerative diseases, including cerebellar ataxia with neuropathy and vestibular areflexia syndrome (CANVAS) (Szmulewicz *et al.*, 2014), ataxia with vitamin E deficiency (AVED) (Yokota *et al.*, 2000), Friedrich's ataxia (Koeppen and Mazurkiewicz, 2013) and some mitochondrial disorders (Lax *et al.*, 2012). However, the causes of approximately half of sensory neuronopathies remain unknown, particularly chronic and slowly progressive sensory neuronopathies (Sghirlanzoni *et al.*, 2005).

In the past decades, multiple genes associated with mitochondrial structure and function have been linked to sensory neuronopathies, including *HADHA* (MIM:600890) in mitochondrial fatty acids β-oxidation (Nadjar *et al.*, 2020), *MT-TK* (MIM: 590060) encoding mitochondrial lysine transfer RNA (Michaud *et al.*, 2020), *FXN* (MIM: 606829) in assembly of iron-sulfur clusters (Koeppen and Mazurkiewicz, 2013), and *POLG* (MIM: 174763) in mtDNA synthesis (Lax *et al.*, 2012). Particularly, pathogenic variants in the *POLG* have been reported to cause autosomal recessive sensory neuronopathy, of which sensory ataxia as a key feature caused by degeneration of dorsal root ganglion and posterior

columns (Lax *et al.*, 2012). However, patients with inherited disease discussed above have a wide spectrum of neurological features, such as ophthalmoparesis, cardiomyopathy, myopathy, psychiatric disorders, cognitive impairment, seizures and encephalopathy. Thus, the hereditary sensory neuronopathy is seen in very rare conditions and easy to be misdiagnosed, which deserves more attention in exploration of probable existence of underlying genetic cause.

COX20 (MIM: 614698) is a chaperone protein involved in the assembly of mitochondrial oxidative phosphorylation (OXPHOS) complex IV [cytochrome c oxidase (COX)], which stabilizes newly synthesized catalytic core subunit COX2 by facilitating the translocating across mitochondrial inner membrane and maintaining interaction with the first transmembrane helix of COX2 (Timon-Gomez *et al.*, 2018). COX20 also interacts directly with SCO1 and SCO2 metallochaperones in maturation of COX2 redox center (Bourens *et al.*, 2014). Variants in *COX20* have been initially associated with complex IV deficiency, an autosomal recessive form of infant-onset mitochondrial disorder that is typically accompanied by growth retardation, hypotonia, and cerebellar ataxia (Szklarczyk *et al.*, 2013). Subsequent studies have broadened the phenotypic spectrum to include milder cases with childhood-onset cerebellar ataxia, dystonia, choreoathetosis and sensory axonal neuropathy (Doss *et al.*, 2014, Otero *et al.*, 2019). More recently, *COX20* variants were identified in two patients from one family with sensory-dominant axonal neuropathy and static encephalopathy (Xu *et al.*, 2019).

Here, we identified bi-allelic pathogenic variants within *COX20* in 8 families showing sensory neuronopathy by whole exome sequencing (WES). Five different *COX20* variants were detected and they were loss-of-function variants leading to decreased level of COX20 protein. Histopathological and functional data further indicated that loss of COX20 caused

impaired mitochondrial complex IV assembly and defective OXPHOS capacity in sensory neuron cell line. Our findings identified a novel causative gene for autosomal recessive sensory neuronopathy and further supported mitochondrial bioenergetic dysfunction as a mechanism in peripheral sensory neuron disease.

Materials and Methods

Subjects

The criteria for enrollment were: 1) autosomal recessive or sporadic; 2) presence of chronic deep sensory loss or sensory ataxia; 3) absence of other features such as upper motor neuron impairment, mental retardation, and cerebellar ataxia; 4) electrophysiological results show non-length-dependent sensory abnormalities that fulfill diagnostic criteria for sensory neuronopathy (Camdessanché *et al.*, 2009); 5) exclusion of acquired causes by routine clinical investigations; 6) pathogenic variants in the causative genes known to be associated with sensory neuronopathies or inherited peripheral neuropathies have been detected by multiplex ligation-dependent probe amplification (MLPA), targeted next-generation sequencing (NGS), and WES in our previous reports (Li *et al.*, 2016, Li *et al.*, 2017, Chen and Dong, 2019, Li *et al.*, 2019, Dong *et al.*, 2020). Genomic DNA was extracted from peripheral EDTA-treated blood using Blood Genomic Extraction Kit (Qiagen). This study was approved by the Ethics Committees in Second Affiliated Hospital in Zhejiang University School of Medicine. All participants signed informed consents prior to enrolment.

Genetic analysis

WES was performed in patients and unaffected family members using Agilent SureSelect^{TM} Human All Exon v6 kit for exome enrichment and the Illumina HiSeq X Ten platform (XY

Biotechnology Co Ltd, Hangzhou, China) for sequencing. Subsequent variant calling, alignment and annotation were performed according to our previously reported protocol (Jiang *et al.*, 2019, Liu *et al.*, 2019). In the consanguineous Family 1, homozygosity mapping was performed by HomozygosityMapper (Seelow *et al.*, 2009) using WES data from index patient(II:3), parents(I:1 and I:2), and her unaffected siblings(II:1 and II:2). As the phenotype in family 1 is inherited in a consanguineous marriage, only those homozygous variants in the index patient that are heterozygous in parents and heterozygous or absent in any of the two unaffected siblings were analyzed. Variants were filtered on the basis of minor allele frequency (MAF) lower than 1% in 1000 Genomes Project (Genomes Project *et al.*, 2015), ExAc (Lek *et al.*, 2016) and gnomAD (Karczewski and Francioli, 2020) database and functional impact on protein change (non-synonymous and/or affecting mRNA splicing variants). Using an overlap-based strategy, we identified the potential causative genes shared by multiple families. Sanger sequencing was performed to validate the potential variants and co-segregation (all primers are listed in the **Supplementary Table 1**). Haplotype analysis was conducted by genotyping 7 single nucleotide polymorphism (SNP) markers flanking *COX20* c.41A>G and covering a region of 0.1 Mb.

Analysis of gene expression

Transcriptomic tissue data generated by the Genotype-Tissue Expression (GTEx) project were used for the expression analysis of *COX20* in human tissues (Consortium, 2015). Single-cell RNA sequencing (scRNA-seq) of the adult mouse brain database (http://mousebrain.org/)(Zeisel *et al.*, 2018) and adult mouse sensory neurons focusing on cell types in dorsal root ganglia (http://linnarssonlab.org/drg/) (Usoskin *et al.*, 2015) were used to analyze the expression distribution patterns of *COX20* and other causative genes associated with sensory neuropathy.

Muscle biopsy and histochemical staining

Skeletal muscle biopsy of the left biceps brachii muscle was performed in patient 1 and patient 4. Skeletal muscle biopsy of the right gastrocnemius muscle and quadriceps femoris muscle were performed in patient 3 and patient 5, respectively. Muscle samples were precooled using isopentane and cryofixed in liquid nitrogen. Transverse sections (8-μm thick) were obtained for routine and enzyme histochemical staining.

Transmission electron microscopy

The muscle samples were immediately fixed with 2.5% glutaraldehyde for 2 h, washed by PBS, and post-fixed in 1% osmium tetraoxide for 2 h. Then the blocks were dehydrated by graded alcohols, embedded in epon, and stained with lead citrate as well as uranyl acetate. Ultrathin sections were cut and viewed through a Transmission electron microscope (Hitachi HT7700, Japan).

Expression plasmids

The wild-type (WT) full-length coding region of human *COX20* cDNA (NM_198076) was cloned into pcDNA3.1-Myc/His vector (Invitrogen). Three missense *COX20* variants identified in this study (p.Lys14Arg, p.Ser33Leu, p.Trp74Cys) and the p.Thr52Pro variant reported previously were introduced into WT *COX20* construct using PCR mutagenesis. After confirming the sequences, they were designated as pcDNA3.1-WT-Myc/His (WT), pcDNA3.1-Lys14Arg-Myc/His (K14R), pcDNA3.1-Ser33Leu-Myc/His (S33L), pcDNA3.1-Thr52Pro-Myc/His (T52P) and pcDNA3.1-Trp74Cys-Myc/His (W74C), respectively.

Cell culture, plasmid transfection and lentiviral transduction

Primary fibroblasts were obtained from a 4-mm skin biopsy of affected patients and normal controls, grown in Dulbecco's Modified Eagle Medium/Nutrient Mixture F-12(DMEM/F12, Gibco) supplemented with 10% fetal bovine serum (Gibco) at 37°C in 5% CO_2. HEK-293T, Hela and ND7/23 cells were cultured at 37°C under 5% CO_2 in DMEM (HyClone) supplemented with 10% fetal bovine serum (Gibco). To determine whether COX20 protein expression and subcellular location were influenced by the variants, HEK-293T and Hela cells were transfected with WT and mutant plasmids with Lipofectamine 3000 reagent (Invitrogen) according to the manufacture's protocol. Forty-eight hours after transfection, transfected cells were collected for further analysis. For COX20 protein stability assay, at 48 h post transfection, cells were treated with 100μg/ml cycloheximide (CHX; Sigma-Aldrich) for 0, 3, 6, and 12 h to evaluate the half-life of the COX20 protein. For protein degradation assay, cells were treated with 100μg/ml CHX and with or without MG132 (20μM, Selleck) for 6 hours. Dimethyl sulphoxide (DMSO) was used as a control vehicle. Lentivirus particles with shRNA specific for *COX20* was purchased from Genomeditech Co. Ltd. ND7/23 cells were transduced with lentivirus and selected with puromycin (2.5 mg/ml) for 4 days. Two cell clones named siCOX20-1 and siCOX20-2 were generated for further experiments.

RNA isolation, quantitation and splicing analysis

For RNA quantification study, total RNA was extracted from control and patient fibroblasts and synthesis of cDNA was performed using the PrimeScript™ II 1st Strand cDNA Synthesis Kit (Takara). Quantitative real-time PCR experiments were further performed using SYBR Premix Ex Taq Kit (Takara) by means of relative quantification ($2^{-\Delta\Delta Ct}$ method). The primer sequences are available in **Supplementary Table 1**. To examine the effect of the c.157+7A>G variant on mRNA splicing, minigene vectors containing either

mutant or WT *COX20* with exon 2 to exon 3 and flanking intron sequence were cloned in pSPL3 vector and transfected into HEK-293T cells. RT-PCR products were visualized in agarose gels and confirmed by Sanger sequencing. To examine the effect of the c.41A>G variant on mRNA splicing, RT-PCR was performed to amplify full length *COX20* transcript using patient fibroblast-derived cDNA. PCR products were visualized in agarose gels and then cloned into pGM-simple-T TA vector (TIANGEN). The vector was transformed into DH5α cells (TIANGEN), and individual colonies were examined and sequenced by Sanger sequencing.

Mitochondrial extraction and membrane fractionation

Mitochondria isolation from cultured cells was performed using mitochondria isolation kit (Beyotime). To separate the peripherally bound membrane proteins and integral membrane proteins, 40μg freshly isolated mitochondria were resuspended in a buffer containing 0.1 M Na_2CO_3, 250 mM sucrose and 0.2 mM EDTA (pH 10.5), incubated for 1 h on ice with gentle nutation and then centrifuged at 20,000 × g for 30 min at 4°C, to separate the supernatant containing the loosely bound membrane proteins and the pellet containing integral membrane proteins. Supernatant and pellet protein samples were analyzed by SDS-PAGE and immunoblotting.

For sub-mitochondrial localization, 40μg freshly isolated mitochondria were resuspended in isotonic buffer containing 250 mM sucrose, 0.2 mM EDTA and 10 mM Tris-HCL (pH 7.4), treated with increasing concentrations of digitonin (0%, 0.1%, 0.125%, 0.150%, 0.175%, 0.20% and 0.25%) for 1 h at 4 °C and then centrifuged at 20,000 × g for 30 min at 4°C, to separate the soluble and insoluble fractions. Soluble and insoluble protein samples were analyzed by SDS-PAGE and immunoblotting.

SDS-PAGE and blue native gel electrophoresis and immunoblotting

Protein samples from HEK-293T cells, fibroblasts and ND7/23 cells were separated by 10% or 12% SDS-polyacrylamide gel electrophoresis (SDS-PAGE) and transferred to polyvinylidene fluoride (PVDF) membranes. Blue native–PAGE (BN-PAGE) was performed as previously described (Jha *et al.*, 2016). Briefly, mitochondria were isolated from cells using mitochondria isolation kit (Beyotime). Fifty micrograms of mitochondrial protein were separated on 4 to 16% Bis-Tris gradient gels (Thermo Fisher Scientific) and transferred onto PVDF membranes. For in-gel measurement of complex activity, gels were incubated with substrate solution overnight at room temperature. The following primary antibodies were used: anti-COX20 (Abcam; ab224570), anti-NDUFA9 (Abclonal; A3196), anti-NDUFA13 (Abcam; ab110240), anti-SDHA (Abcam; ab14715), anti-UQCRC2 (Abcam; ab14745), anti-COX1 (Abcam; ab14705), anti-COX2 (Abcam; ab79393), anti-ATP5A (Abcam; ab14748), anti-VDAC1 (Abcam; ab14734), anti-TOM20 (Cell Signaling Technology; 42406S), anti-Myc (Cell Signaling Technology; 2276S), anti-GAPDH (Cell Signaling Technology; 8884S), and anti-β-Tubulin (Cell Signaling Technology; 5346S). The gray values of the bands were analyzed using Adobe Photoshop software.

Immunofluorescence analysis

Hela cells transiently transfected with Myc-tagged COX20 were cultured in glass-bottomed dishes. After 24 hours of transfection, cells were fixed with 4% paraformaldehyde for 20 min at room temperature and blocked in PBS containing 0.1% TritonX-100 and 5% bovine serum albumin for 60 minutes. Cells were then incubated with anti-Myc (1:1000, Sigma) antibody and anti-COX2 (1:200, Abcam) in the blocking buffer at 4°C overnight, followed by secondary anti-mouse IgG Alexa Fluor488 and anti-rabbit IgG Alexa Fluor 596 antibodies (1:1000, Life Technologies). Cell nuclei were then stained with 40, 6-diamidino-

2-phenylindole (DAPI; 1:5000, Life Technologies). Fluorescence images were captured by Olympus FV3000 confocal system.

High-resolution respirometry

The Oxygraph-2k (O2k; OROBOROS Instruments) was used for measuring mitochondrial respiration (Djafarzadeh and Jakob, 2017). For measuring C (OCR), two million cells were added to each chamber filled with 2 mL of cell culture media. Oligomycin, Carbonyl cyanide 4-(trifluoromethoxy) phenylhydrazone (FCCP), and rotenone + antimycin A were injected sequentially to each chamber. Oligomycin inhibited ATP synthase and provided information on decreased OCR (ATP-linked respiration). FCCP uncoupled oxygen consumption from ATP production and enabled maximal rates of electron transport to occur to raise OCR to a maximal value (maximal respiration capacity). Rotenone and Antimycin A blocked complexes I and III and reduced OCR to a minimal value (non-mitochondrial respiration). For measuring mitochondrial complex I, II+III, IV associated oxygen consumption rate, 50μg freshly isolated mitochondria were added to each chamber. Substrate-uncoupler-inhibitor-titration (SUIT) protocols were assayed as detailed elsewhere (Djafarzadeh and Jakob, 2017). In brief, with the presence of pyruvate, malate and glutamate (PMG), substrate-driven OCR was measured for complex I (addition of ADP followed by rotenone, an inhibitor of complex I), complex II+III (addition of succinate followed by antimycin A, an inhibitor of complex III), and complex IV [addition of N, N, N′, N′-tetramethyl-p-phenylenediamine (TMPD)/ascorbate followed by azide, an inhibitor of complex IV].

Assessment of mitochondrial membrane potential

Cells were stained with 100 nM tetramethyl rhodamine methyl ester (TMRM; Invitrogen) for 0.5 h at 37°C and the fluorescence signal was detected with Olympus fluorescence microscope (excitation/emission 525/590 nm). Image-J software was used for quantification of the cell number and fluorescence intensity. Quantification was performed in four random visual fields of at least 100 cells from three independent experiments.

Mitochondrial respiratory complex IV activity microplate assay

Abcam's Complex IV Human Enzyme Activity Microplate Assay Kit (ab109909) were used to quantitatively measure the activity of mitochondrial respiratory complex IV from fibroblast extracts. The assay followed the protocol suggested by the manufacturer.

Cell proliferation and viability assay

For cell proliferation assay, the cells were cultured in a 96-well plate at a density of 2000 cells/well and incubated with 25mM glucose DMEM or no-glucose DMEM supplemented with 10 mM galactose for 4 days. The proliferation of cells in different media of glucose and galactose were assessed every 24 hours using the Cell Counting Kit-8 (Beyotime). Growth rate was determined by the ratio of absorbance with specified medium for 4 days to absorbance seeded initially. For cell viability assay, the cells were cultured in a 96-well plate at a density of 10,000 cells/well and incubated with hydrogen peroxide (200μM) for one hour before measuring the absorbance. The absorbance was measured at 450 nm using SpectraMax 190 microplate reader (Molecular Devices).

Statistical analysis

Data are presented as the mean ± SD. The following convention was used: *p <0.05; **p <0.01; ***p <0.001; ****p<0.0001; ns, not significant. Student's t-test and one-way

ANOVA in either 2 or multiple groups for statistical significance were performed using GraphPad Prism 7 software.

Data availability

The datasets generated and/or analyzed during the current study are available from the corresponding author on reasonable request.

Results

Identification of bi-allelic *COX20* variants

WES were performed in all 14 patients and homozygosity mapping was performed in the consanguineous family (Family 1 in **Fig. 1A**). A total of 28 shared homozygous regions > 1 Mb was identified. We specifically looked for potential pathogenic variants located within these regions and present in multiple families. We identified a homozygous variant c.41A>G (p. Lys14Arg) within *COX20* in three families (Family 1-3 in **Fig. 1A**). Compound heterozygous variants including c.41A>G/c.222G>T (p.Trp74Cys), c.41A>G/c.98C>T (p.Ser33Leu), c.41A>G/ c.157+7A>G and c.41A>G/c.259C>T (p.Gln87*) were identified in 5 additional families, respectively (Family 4-8 in **Fig. 1A**). These variants were also confirmed by Sanger sequencing (**Fig. 1B**) and co-segregated with phenotypes within these families. Allele frequency in population and *in silico* prediction of 5 variants were summarized in **Supplementary Table 2**. These variants were extremely rare in global human genome databases and located at evolutionarily highly conserved amino acid residues (**Fig. 1C**). Although c.41A>G(p.Lys14Arg) variant was predicted as benign in three *in silico* missense predictions, it was predicted to cause abnormal splicing by abolishing the donor splice site of exon 1 (dbscSNV score=0.998) (Jian *et al.*, 2014).

Founder effect of c.41A>G variant

The c.41A>G (p.Lys14Arg) was the most common variant in our cohort and present in all 8 Chinese Han families from eastern China (7 in Zhejiang province and 1 in Jiangxi province). The allele frequency of the variant c.41A>G is 0.00132 in the Chinese population based on ChinaMAP database (Cao *et al.*, 2020) (28 of 21176 alleles examined) and 0.00103 in the eastern Chinese population based on our in-house exomes database (2 of 1934 alleles examined). In comparison, the allele frequency was 0.00003552 based on an allelic count of 5 out of 140748 genomes in the gnomAD v3 database (only one female individual of East Asian ancestry who is heterozygous for the variant), much lower than that in eastern Chinese population. The genomic data supported a hypothesis that the c.41A>G was a founder variant in the eastern Chinese population. We further performed haplotype analysis and a unique haplotype of 106kb in size containing c.41A>G variant gene was identified in all 8 families, suggesting it was a founder variant (**Supplementary Table 3**).

Clinical features

Altogether, we identified 8 index cases with bi-allelic variants in *COX20*. Of note, 7(87.5%) cases were sporadic, with no evidence of a family history or consanguinity. All patients had similar clinical features and electrophysiological findings characterized by sensory neuronopathy. The mean age of disease onset was 8.2 ± 6.3 (range 1-17) years with the walking difficulty as the most common complaint at onset. Four patients (50%) suffered from delayed motor milestones, and 7 (87.5%) reported pes cavus **(Fig. 2A**), indicating that neuropathy probably started earlier in their life. All patients exhibited impaired balance with stomping gait. Five (62.5%) patients showed relatively mild limb weakness and 2 (25%) showed muscle atrophy in distal lower limbs (patient 1 and 4 in **Fig. 2A**). Reduced deep tendon reflex and vibratory sensation, and positive Romberg sign were observed in all 8 patients. Magnetic resonance imaging (MRI) of spinal cord showed severe spinal cord

atrophy with no intrinsic signal abnormality in patient 2 and 5 (**Fig. 2B**). Brain MRI showed mild cerebral atrophy in patient 4 (**Supplementary Fig. 1A**), while no remarkable change was observed in other patients. Nerve conduction studies showed global absent or severe decreased sensory nerve action potential (SNAP) in four limbs with normal or mildly abnormal motor nerve conduction studies (**Table 1**), indicating that ataxia symptoms were attributable to sensory ataxia. With CMT neuropathy score (CMTNS), clinical severity was mild (score 0-10) in 5 (62.5%), moderate (score 11-20) in 2 (25%), and severe (score >20) in one patient. Laboratory studies showed normal lactate and pyruvate levels in blood or CSF and serum creatine kinase levels. The detailed clinical features for these patients are shown in **Table 2** and **supplementary data**.

Histopathological features

Sural nerve biopsy in patient 5 showed marked loss of large and medium myelinated fibers and chronic axonal degeneration (data not shown). Muscle samples were taken from patients 1, 3, 4 and 5. HE staining revealed no significant endomysial or perimysial fibrosis, no regeneration and necrosis had been found. On modified Gomori trichrome staining, neither ragged-red fibers nor nemaline bodies were seen. Additionally, there were no abnormal signs in cytochrome c oxidase (COX) staining, succinate dehydrogenase (SDH) staining, Nicotinamide adenine dinucleotide-tetrazolium reductase (NADH-TR) staining (**Fig. 2C and Supplementary Fig. 1B, C and D)**. Results of electron microscope analyses revealed that numerous mitochondria had abnormal internal organization with vacuoles and concentric lamellae (**Fig. 2D and E**), which was suggestive of mitochondrial abnormalities.

Minigene splicing analysis of c.157+7A>G variant

As the patient-derived RNA of c.157+7A>G variant was not available, we developed a minigene assay to examine the effect of this variant on *COX20* splicing **(Supplementary Fig. 2A)**. Gel electrophoresis of mutant PCR products showed a shorter band with exon 2 skipped splicing pattern confirmed by sequencing **(Supplementary Fig. 2B)**. The c.157+7A>G variant therefore caused the skipping of exon 2 resulting in a premature stop codon p.Ser15Valfs*11.

Expression analysis of missense variants

To elucidate the biological effects of the three missense variants, C-terminal myc-tag plasmids expressing WT, K14R, S33L, W74C, or T52P-COX20 protein were constructed. The p.Thr52Pro variant was previously reported to cause COX20 protein depletion (Doss *et al.*, 2014), it was used as a positive control in the experiment. Western blot analysis revealed that S33L-COX20 and W74C-COX20 expression were significantly decreased compared to WT-COX20 (declined approximately 50% and 70%), whereas the p.Lys14Arg variant did not affect the protein level **(Fig. 3A and B)**.

The c.41A>G (p.Lys14Arg) lies within the donor splice site of exon 1. To assess its impact on splicing, PCR was performed on cDNA synthesized from control's and patients' fibroblast RNA. TA clone sequencing identified that this amplicon lacked 20 base pairs at the 3' end of exon 1, indicating the use of an upstream donor splice site within exon 1. The missense c.41A>G (p.Lys14Arg) variant therefore produced abnormal splicing and caused a premature stop codon p.Gly8Valfs*2 (**Fig. 3C and D**). In addition, *COX20* mRNA level in patients with homozygous or heterozygous c.41A>G (p.Lys14Arg) were significantly decreased (**Fig. 3E**), indicating that shortened transcript was instable and eliminated by nonsense-mediated mRNA decay (NMD). A substantial decrease in COX20 protein level was identified in corresponding patient-derived fibroblasts compared to control fibroblasts

(Fig. 3F and G), but protein level of important interacting protein, COX2, was not affected **(Fig. 3F and H)**.

We further used cycloheximide (CHX), a protein synthesis inhibitor, to measure the protein degradation rates of S33L and W74C-COX20. As shown in **Supplementary Fig. 2C and D**, mutant COX20, especially W74C-COX20, were degraded faster than WT, suggesting that two missense variants affected protein half-life of COX20. We then evaluated the role of the ubiquitin-proteasome system (UPS) in degradation of mutant proteins. We found that MG132 treatment rescued the degradation of already synthesized mutant proteins, particularly in S33L-COX20 **(Supplementary Fig. 2E, F, G, H and I)**.

Wild-type and mutant COX20 localizes to the inner mitochondrial membrane

To clarify whether the subcellular localization of COX20 was affected by variants in transmembrane domain of COX20 (p.Ser33Leu and p.Trp74Cys). Both WT and mutant COX20 proteins were enriched in mitochondria-rich fractions (**Fig. 3I**), and co-localized with inner mitochondrial membrane (IMM) marker COX2 in HeLa cell (**Fig. 3J**). To further determine the sub-mitochondrial location, we first established that both WT and mutant COX20 were membrane-bound protein by sodium carbonate extraction (**Fig. 3K**). Then, we determined that both WT and mutant COX20 showed a similar digitonin extraction pattern with IMM marker COX2 by extracting COX20 from mitochondria using increasing concentrations of digitonin (**Fig. 3L**). Taken together, these observations indicated that mutant COX20 was still being targeted to the mitochondria and resided in IMM, not in the outer mitochondrial membrane (OMM).

Expression of *COX20* in tissues and cell types

Because pathogenic variants in *COX20* gene caused predominant proprioceptive sensory loss and ataxia (indicating damage of large neurons) in our patients rather than a multisystem neurological impairment of mitochondrial disease, we next explored whether the tissue-specific susceptibility resulted from preferential expression of *COX20*. We investigated these differences in silico using public bulk tissue and sensory neuron cell-specific transcriptomic data. In the GTEx project, the RNA tissue category revealed that *COX20* is expressed in multiple human tissues including nerve and brain (**Fig. 4A**), with evidence for highest expression in peripheral nervous system neurons while low expression in Schwann cells based on scRNA-seq data of mouse nervous system (**Fig. 4B**). In a scRNA-seq database that focused on cell types in dorsal root ganglia, *COX20* was preferentially expressed in two proprioceptive populations (termed NF4 and NF5). We also noticed a high expression level of other causative genes associated with similar phenotypes, such as *POLG*, *TTPA* and *FAM134B*, in NF5 cells (**Fig. 4C**).

COX20 deficiency impairs COX assembly and enzymatic activity

COX20 is a critical chaperone for the assembly of COX, but the pathophysiological impacts for loss of COX20 have been not systematically studied in neuron. To address the functional role of COX20 in sensory neuronopathy, we used lentiviral-mediated shRNA to generate the COX20-silenced ND7/23 cell line, which was derived from mouse sensory neurons in dorsal root ganglia. Two COX20-silenced ND7/23 cell clones, siCOX20-1 and siCOX20-2, were used for further experiments (**Fig. 5A and B**). Western blot of isolated mitochondria lysates in siCOX20 cells revealed a marked reduction of OXPHOS complex IV subunit (COX1) (**Fig. 5C and D**), which was associated with a decrease in the steady-state levels of assembled complex IV (CIV), as demonstrated by BN-PAGE (**Fig. 5E and F**). BN-PAGE showed that COX20 silencing produced an isolated CIV assembly defect. A

significant reduction of CIV was observed in the siCOX20-2 cells, but not in siCOX20-1 cells possibly due to its relatively low knockdown efficiency. In-gel CIV activity staining was also reduced (**Fig. 5G**), the loss of enzymatic activity was correlated with a reduction in the amount of complex IV subunits. Consistent with these observations, the oxygen consumption rate of complex IV substrate-driven respiration measured by high-resolution respirometry was reduced in siCOX20 cells (**Fig. 5H**).

COX20 deficiency affects mitochondrial bioenergetics and inhibits cell growth

To investigate whether the impairment of OXPHOS complex IV assembly affects cellular bioenergetics, we measured the OCRs in siCOX20 cells. As shown in **Fig. 5I** and **J**, knockdown of COX20 expression resulted in the reduction of ATP-linked OCR and maximal respiration OCR, indicating a lower spare respiratory capacity. No differences were detected in proton leak OCR and non-mitochondrial OCR. The mitochondrial membrane potential, the driving force for mitochondrial ATP production, is a key indicator for healthy mitochondria. TMRM accumulates in active mitochondria with intact membrane potentials. As shown in **Fig. 5K** and **L**, the signals of TMRM in two COX20 silenced cells ranged from 4% to 18%, with a significant decrease against controls, indicating depolarization of the mitochondrial membrane. To determine whether the reduced spare respiratory capacity and the subsequent mitochondrial dysfunction affected cell growth and viability, cells were cultured in galactose medium to promote energy metabolism toward oxidative phosphorylation. As shown in **Fig. 5M**, growth rate was significantly lower in siCOX20 cells than that in control cells in regular glucose medium, and further decreased in oxidative phosphorylation-promoting galactose media. Incubation with the oxidative stressor hydrogen peroxide (200μM) for one hour significantly suppressed the cell viability in siCOX20-2 cells (**Fig. 5N**). Taken together, these findings indicated that silencing of the

COX20 gene in sensory neurons disrupted cell energy metabolism. Therefore, the abnormal mitochondrial function was the potential pathogenic mechanisms underlying sensory neuronopathy.

Characterization of mitochondrial defects in cultured fibroblasts from patients

To validate these mitochondrial defects in patients' fibroblasts, fibroblasts from one control individual, patient 1 with homozygous pathogenic variant, and patient 5 with compound heterozygous pathogenic variants in *COX20* gene were cultured. BN-PAGE revealed decreased levels of assembled complex IV in affected subjects compared to the control subject (**Fig. 6A, B, C and D**). This was associated with a decrease in complex IV enzyme activity in patients' fibroblasts, as demonstrated by mitochondrial complex IV enzyme assays (**Fig. 6E**). Measurement of oxygen consumption rate using Oxygraph-2k respirometer revealed significant reduction in basal, ATP-linked, maximal respiration, and spare capacity in patients' fibroblasts (**Fig. 6F and G**). These findings were compatibly similar to the results in the knockdown cells, demonstrating the *COX20* variants identified in our patients resulted in the reduced complex IV assembly and mitochondrial bioenergetic dysfunction.

Discussion

In this study, we provided a combination of genetic, histopathological, electrophysiological and functional evidence to support that *COX20* gene was a novel causative gene for autosomal recessive sensory neuronopathy. Genetically, missense, nonsense, and splice site variants in *COX20* were identified in 8 autosomal-recessive families. They were novel or extremely rare variants in public databases and predicted to be pathogenic. These variants led to decreased level of COX20 protein, impaired mitochondrial complex IV assembly,

and defective OXPHOS capacity. Patients with *COX20* variants showed early onset and slowly progressive deep sensory loss and sensory ataxia.

Genetic data from our cohort as well as from control databases suggested that the predominant pathogenic variant, c.41A>G (p.Lys14Arg), with a carrier frequency of ~2 per 1,000 individuals, was the founder variant in eastern China as the most common genetic cause of in our patients. Therefore, we suggest that *COX20* should be considered in the molecular diagnostic evaluation of patients with sensory neuronopathy, the following features should help to prioritize *COX20* for genetic analysis: 1) autosomal recessive or sporadic pedigree; 2) early-onset progressive sensory ataxia, loss of position and vibration sense, absent tendon reflexes; 3) nerve conduction studies show widespread loss or low amplitude of sensory-nerve action potentials with non-length-dependent pattern. Motor nerve conduction study findings are normal or mildly decreased.

The most common variant c.41A>G (p.Lys14Arg) was previously reported in compound heterozygous state in four patients who presented with hypotonia, dystonia, dysarthria, ataxia, and sensory neuropathy (Otero *et al.*, 2019). More recently, c.41A>G (p.Lys14Arg) variant was identified in a Chinese family with autosomal recessive sensory-dominant axonal neuropathy and static encephalopathy characterized by dysesthesia, limb weakness, dysarthria and cognitive deficits (Xu *et al.*, 2019). The clinical presentations of these patients showed some overlaps in central and peripheral nervous systems. However, our patients presented predominant proprioceptive sensory loss and sensory ataxia rather than a multisystem neurological impairment. Preferential expression of *COX20* in proprioceptive neurons may provide a potential explanation for the tissue-specific manifestation. However, the mechanism underlying the phenotypic variability between our patients and Turkish or American patients is still unclear. Notably, it seems that expression

level of COX20 has little correlation with the interfamilial differences in phenotypes, because we have observed that almost no COX20 protein expression in our patients with homozygous c.41A>G (p.Lys14Arg) variant, consistent with previous reports (Otero *et al.*, 2019, Xu *et al.*, 2019). Further investigation is needed to confirm whether the expression level of COX20, race specific modifier genes or epigenetic factors play a role in the determination of phenotypes.

To date, several genes related to mitochondrial functions have been identified as causative genes of sensory neuronopathies or mitochondrial disorders with sensory neuronopathy as a key feature. For example, pathogenic variants in *POLG* have been reported to cause sensory neuronopathy by defects in mitochondrial complex I and IV deficiency secondary to mtDNA deletion and depletion (Lax *et al.*, 2012). COX20, as a nuclear-encoded assembly factor, plays an important role in mitochondrial complex IV function. Previous studies have showed that TALENs-mediated knockout of COX20 in HEK-293T cell results in a profound decrease in CIV levels and activity by destabilizing COX2 and subsequent block in the incorporation of COX2 into CIV assembly S2 intermediate (Bourens *et al.*, 2014). Consistent with these findings, we showed that knockdown of COX20 caused impaired COX assembly and reduced COX activity in ND7/23 cell. In addition, a recent study showed that deletion of COX20 in yeast cells resulted in intolerance to hydrogen peroxide induced oxidative stress and programmed cell death (Keerthiraju *et al.*, 2019). In our cell model, we have also found that COX20 deficiency induced slow cell growth and decreased cell viability under oxidative stress. Thus, we hypothesized that the pathogenic variants of *COX20* are associated with the disease by affecting the assembly and maturation of COX with a reduction of CIV activity, mitochondrial membrane potential depolarization, compromised respiration and tolerance

to oxidative stress by loss of COX20 protein. We here provided preliminary evidence to further support mitochondrial dysfunction having a direct effect on the pathophysiology of peripheral neuropathies.

Although the precise molecular mechanisms linking COX deficiency to sensory neuronopathy remain to be clarified, studies on complex IV deficiency with neuropathy or Charcot-Marie-Tooth disease causative genes encoding COX associated mitochondrial proteins such as *COA3*, *COA7*, *SURF1*, *SCO2* and *COX6A1* suggested that impaired axonal transport, oxidative stress and defective mitochondrial copper homeostasis might be involved (Echaniz-Laguna *et al.*, 2013, Tamiya *et al.*, 2014, Ostergaard *et al.*, 2015, Higuchi *et al.*, 2018, Rebelo *et al.*, 2018). Further work is needed to clarify the role of *COX20* in causing the neurodegeneration of the large proprioceptive sensory neurons and to precisely establish the tissue-specific cellular signaling pathways that can be altered by COX deficiency.

In summary, we identified bi-allelic pathogenic variants in *COX20* causing autosomal recessive sensory neuronopathy, expanding genotype and phenotype spectrums of *COX20* gene. Moreover, histopathological and functional data further indicated that loss of COX20 contributed to mitochondrial bioenergetics dysfunction as a loss-of-function mechanism in sensory neuronopathies.

Acknowledgements

We would like to thank the patients and their family members for participating in this study.

Funding

This study was supported by the grant from the National Natural Science Foundation of China to Z-Y.W. (81671245), the research foundation for distinguished scholar of Zhejiang

University to Z-Y.W. (188020-1938 10101/089) and the Fundamental Research Funds for the Central Universities (2019XZZX001-01-04).

Competing interests

The authors report no competing interests.

Supplementary material

Supplementary material is available at *Brain* online.

References

Bourens M, Boulet A, Leary SC, Barrientos A. Human COX20 cooperates with SCO1 and SCO2 to mature COX2 and promote the assembly of cytochrome c oxidase. Hum Mol Genet 2014;23(11):2901-13.

Camdessanché JP, Jousserand G, Ferraud K, Vial C, Petiot P, Honnorat J, et al. The pattern and diagnostic criteria of sensory neuronopathy: a case-control study. Brain 2009;132(Pt 7):1723-33.

Cao Y, Li L, Xu M. The ChinaMAP analytics of deep whole genome sequences in 10,588 individuals. Cell Res 2020;Advance online publication.

Chen CX, Dong HL. Genetic spectrum and clinical profiles in a southeast Chinese cohort of Charcot-Marie-Tooth disease. Clin Genet 2019;96(5):439-48.

Consortium G. Human genomics. the genotype-tissue expression (GTEx) pilot analysis: multitissue gene regulation in humans. Science 2015;348(6235):648-60.

Damasceno A, França MC, Jr., Nucci A. Chronic acquired sensory neuron diseases. Eur J Neurol 2008;15(12):1400-5.

Djafarzadeh S, Jakob SM. High-resolution respirometry to assess mitochondrial function in permeabilized and intact cells. J Vis Exp 2017;120(54985):54985.

Dong HL, Wei Q, Li JQ, Li HF, Bai G, Ma H, et al. Genetic spectrum of MCM3AP and its relationship with phenotype of Charcot-Marie-Tooth disease. J Peripher Nerv Syst 2020;25(2):107-11.

Doss S, Lohmann K, Seibler P, Arns B, Klopstock T, Zuhlke C, et al. Recessive dystonia-ataxia syndrome in a Turkish family caused by a COX20 (FAM36A) mutation. J Neurol 2014;261(1):207-12.

Echaniz-Laguna A, Ghezzi D, Chassagne M, Mayençon M, Padet S, Melchionda L, et al. SURF1 deficiency causes demyelinating Charcot-Marie-Tooth disease. Neurology 2013;81(17):1523-30.

Genomes Project C, Auton A, Brooks LD, Durbin RM, Garrison EP, Kang HM, et al. A global reference for human genetic variation. Nature 2015;526(7571):68-74.

Gwathmey KG, Pearson KT. Diagnosis and management of sensory polyneuropathy. BMJ 2019;365:l1108.

Higuchi Y, Okunushi R, Hara T, Hashiguchi A, Yuan J, Yoshimura A, et al. Mutations in COA7 cause spinocerebellar ataxia with axonal neuropathy. Brain 2018;141(6):1622-36.

Jha P, Wang X, Auwerx J. Analysis of mitochondrial respiratory chain supercomplexes using blue native polyacrylamide gel electrophoresis (BN-PAGE). Curr Protoc Mouse Biol 2016;6(1):1-14.

Jian X, Boerwinkle E, Liu X. In silico prediction of splice-altering single nucleotide variants in the human genome. Nucleic Acids Res 2014;42(22):13534-44.

Jiang B, Zhou J, Li HL, Chen YG, Cheng HR, Ye LQ, et al. Mutation screening in Chinese patients with familial Alzheimer's disease by whole-exome sequencing. Neurobiol Aging 2019;76:215.e15-.e21.

Karczewski KJ, Francioli LC. The mutational constraint spectrum quantified from variation in 141,456 humans. Nature 2020;581(7809):434-43.

Keerthiraju E, Du C, Tucker G, Greetham D. A role for COX20 in tolerance to oxidative stress and programmed cell death in Saccharomyces cerevisiae. Microorganisms 2019;7(11):575.

Koeppen AH, Mazurkiewicz JE. Friedreich ataxia: neuropathology revised. J Neuropathol Exp Neurol 2013;72(2):78-90.

Lax NZ, Whittaker RG, Hepplewhite PD, Reeve AK, Blakely EL, Jaros E, et al. Sensory neuronopathy in patients harbouring recessive polymerase gamma mutations. Brain 2012;135(Pt 1):62-71.

Lax NZ, Whittaker RG, Hepplewhite PD, Reeve AK, Blakely EL, Jaros E, et al. Sensory neuronopathy in patients harbouring recessive polymerase γ mutations. Brain 2012;135(Pt 1):62-71.

Lek M, Karczewski KJ, Minikel EV, Samocha KE, Banks E, Fennell T, et al. Analysis of protein-coding genetic variation in 60,706 humans. Nature 2016;536(7616):285-91.

Li JQ, Dong HL, Chen CX, Wu ZY. A novel WARS mutation causes distal hereditary motor neuropathy in a Chinese family. Brain 2019;142(9):e49.

Li LX, Liu GL, Liu ZJ, Lu C, Wu ZY. Identification and functional characterization of two missense mutations in NDRG1 associated with Charcot-Marie-Tooth disease type 4D. Hum Mutat 2017;38(11):1569-78.

Li LX, Zhao SY, Liu ZJ, Ni W, Li HF, Xiao BG, et al. Improving molecular diagnosis of Chinese patients with Charcot-Marie-Tooth by targeted next-generation sequencing and functional analysis. Oncotarget 2016;7(19):27655-64.

Liu ZR, Dong HL, Ma Y, Wu ZY. Identification and functional characterization of mutations within HADHB associated with mitochondrial trifunctional protein deficiency. Mitochondrion 2019;49:200-5.

Michaud M, Stojkovic T, Maisonobe T, Behin A, Rucheton B, Léonard-Louis S, et al. Ganglionopathies Associated with MERRF Syndrome: An Original Report. J Neuromuscul Dis 2020;Advance online publication.

Nadjar Y, Souvannanorath S, Maisonobe T, Brisset M, De Lonlay P, Schiff M, et al. Sensory neuronopathy as a major clinical feature of mitochondrial trifunctional protein deficiency in adults. Rev Neurol (Paris) 2020;176(5):380-6.

Ostergaard E, Weraarpachai W, Ravn K, Born AP, Jønson L, Duno M, et al. Mutations in COA3 cause isolated complex IV deficiency associated with neuropathy, exercise intolerance, obesity, and short stature. J Med Genet 2015;52(3):203-7.

Otero MG, Tiongson E, Diaz F, Haude K, Panzer K, Collier A, et al. Novel pathogenic COX20 variants causing dysarthria, ataxia, and sensory neuropathy. Ann Clin Transl Neurol 2019;6(1):154-60.

Rebelo AP, Saade D, Pereira CV, Farooq A, Huff TC, Abreu L, et al. SCO2 mutations cause early-onset axonal Charcot-Marie-Tooth disease associated with cellular copper deficiency. Brain 2018;141(3):662-72.

Seelow D, Schuelke M, Hildebrandt F, Nurnberg P. HomozygosityMapper--an interactive approach to homozygosity mapping. Nucleic Acids Res 2009;37(Web Server issue):W593-9.

Sghirlanzoni A, Pareyson D, Lauria G. Sensory neuron diseases. Lancet Neurol 2005;4(6):349-61.

Szklarczyk R, Wanschers BF, Nijtmans LG, Rodenburg RJ, Zschocke J, Dikow N, et al. A mutation in the FAM36A gene, the human ortholog of COX20, impairs cytochrome c oxidase assembly and is associated with ataxia and muscle hypotonia. Hum Mol Genet 2013;22(4):656-67.

Szmulewicz DJ, McLean CA, Rodriguez ML, Chancellor AM, Mossman S, Lamont D, et al. Dorsal root ganglionopathy is responsible for the sensory impairment in CANVAS. Neurology 2014;82(16):1410-5.

Tamiya G, Makino S, Hayashi M, Abe A, Numakura C, Ueki M, et al. A mutation of COX6A1 causes a recessive axonal or mixed form of Charcot-Marie-Tooth disease. Am J Hum Genet 2014;95(3):294-300.

Timon-Gomez A, Nyvltova E, Abriata LA, Vila AJ, Hosler J, Barrientos A. Mitochondrial cytochrome c oxidase biogenesis: Recent developments. Semin Cell Dev Biol 2018;76:163-78.

Usoskin D, Furlan A, Islam S, Abdo H, Lonnerberg P, Lou D, et al. Unbiased classification of sensory neuron types by large-scale single-cell RNA sequencing. Nat Neurosci 2015;18(1):145-53.

Xu H, Ji T, Lian Y. Observation of novel COX20 mutations related to autosomal recessive axonal neuropathy and static encephalopathy. Hum Genet 2019;138(7):749-56.

Yokota T, Uchihara T, Kumagai J, Shiojiri T, Pang JJ, Arita M, et al. Postmortem study of ataxia with retinitis pigmentosa by mutation of the alpha-tocopherol transfer protein gene. J Neurol Neurosurg Psychiatry 2000;68(4):521-5.

Zeisel A, Hochgerner H, Lönnerberg P, Johnsson A, Memic F, van der Zwan J, et al. Molecular architecture of the mouse nervous system. Cell 2018;174(4):999-1014.e22.

Legends of Figures

Figure 1. Bi-allelic variants in *COX20* in eight unrelated autosomal recessive sensory neuronopathy families. (A) The pedigree structure and segregation analyses of family 1 to 8. Squares represent males and circles represent females. The arrow indicates the proband. (B) Sequencing chromatograms of five identified variants. The upper chromatograms represent normal sequences and lower ones represent mutant sequences. Red box indicates

the variant site. (C) Distribution of variants across *COX20* gene and amino acid conservation of COX20 polypeptide in different species. The variant c.41A>G (p.Lys14Arg) in exon 1, highlighted in red box, was identified at a particularly high frequency. Lys14, Ser33, Trp74 and Gln87 are highly conserved in different species.

Figure 2. Clinical and histopathological features in patients. (A) Atrophy of muscles in the feet and pes cavus seen in patient 1, 3, 4, 5. (B) Sagittal and axial T2-weighted images of the spine of patient 2 and 5 showed spinal cord atrophy. (C) Histochemical analysis of the quadriceps femoris muscle from patient 5 revealed no abnormal signs in cytochrome c oxidase (COX) staining, modified Gomori trichrome (MGT) staining, succinate dehydrogenase (SDH) staining, Nicotinamide adenine dinucleotide-tetrazolium reductase (NADH-TR) staining. Scale bars represent 100 μm. (D-E) Electron micrographs of longitudinal sections of muscle from patient 3 (left) and patient 5 (right) exhibited abnormal mitochondrial internal organization with vacuoles and concentric lamellae (red box). Scale bars represent 1 μm (D) and 0.5 μm (E), respectively.

Figure 3. *COX20* variants disrupt the expression level. (A and B) Overexpression of the recombinant WT and mutant Myc tagged COX20 in HEK-293T cells. Western blot analysis showed significant decrease in COX20 levels in the S33L, W74C, T52P-COX20 relative to WT-COX20. Data are shown as means ±SD (n=3). ****p<0.0001; n.s. = not significant. (C and D) Exon-intron architecture, mRNA maturation, and sequence diagrams of wild-type (WT) *COX20* transcript (lower) and abnormal spliced transcript (upper) resulting from skipping of 20 base pairs at the 3' end of exon 1. (E) qPCR analysis revealed a significantly decreased expression of *COX20* mRNA in the patient 1 and 5 fibroblasts. Data are shown as means ±SD (n=3). ***p<0.001; ****p<0.0001. (F) Expression levels of COX20 and COX2 protein in the fibroblasts of the two patients and control individual. (G) Western blot

analysis revealed COX20 protein was significantly reduced in the patient 1 and 5 fibroblasts. Data are shown as means ±SD (n=3). ***p<0.001; ****p<0.0001. (H) Western blot analysis revealed COX2 protein was not affected in the fibroblasts of patient 1 and 5. Data are shown as means ± SD (n=3). n.s. = not significant. (I) Mitochondria and cytosol fractions were extracted from HEK-293T cells transfected with WT or mutant COX20. Protein expression is determined by western blot using antibodies against Myc, TOM20 (mitochondria), and Tubulin (cytosol). (J) Subcellular localization of WT and mutant COX20 in Hela cells. Confocal images of Myc (green), COX2 (red), DAPI nuclear staining (blue), and merged signals. Scale bars represent 20 μm. (K) Extraction of WT or mutant COX20 from HEK-293T mitochondria with buffer alone, Na_2CO_3 solution or buffer containing 1% Triton X-100. S = supernatant; P = pellet. COX2 is integral membrane protein, ATP5A is peripherally bound membrane protein, HSP60 is in the matrix. (L) Extraction of WT or mutant COX20 from HEK-293T mitochondria using increasing concentrations of digitonin. TOM20 is outer mitochondrial membrane (OMM) protein, COX2 is inner mitochondrial membrane (IMM) protein.

Figure 4. Expression of *COX20* in tissues and cell types. (A) Expression of *COX20* across multiple human tissues. Data were generated by the GTEx Consortium. RPKM = Reads Per Kilobase per Million mapped reads. (B) Expression of *COX20* across single cells isolated from mouse central nervous system (CNS) and peripheral nervous system (PNS). Data were generated by scRNA-seq and displayed by a heatmap. HC = hippocampus; MSN = medium spiny neurons; NBL = neuroblasts; OB = olphactory bulb; Symp = sympathetic. (C) Expression of *COX20* and other hereditary sensory neuropathy causative genes across single sensory neuron cells isolated from mouse dorsal root ganglia. Data were generated by scRNA-seq and displayed by a heat map. Sensory neuron cells comprising the four principal

neuronal types. NF = neurofilament containing; NP = non-peptidergic nociceptors; PEP = peptidergic nociceptors; TH = tyrosine hydroxylase containing.

Figure 5. COX20 deficiency impairs COX assembly, enzymatic activity and mitochondrial bioenergetics in knockdown cells. (A and B) Immunoblotting showed strong reduction of COX20 expression by lentiviral-mediated shRNA knockdown in siCOX20-1 and siCOX20-2 relative to siCtrl. Data are shown as means ±SD (n=3). ***p<0.001. (C and D) SDS-PAGE western blot of isolated mitochondria showed reduced levels of CIV subunit (COX1) in siCOX20-1 and siCOX20-2 relative to siCtrl. VDAC1 is indicative of loading. Data are shown as means ±SD (n=3). *p<0.05; **p<0.01; n.s. = not significant. (E and F) BN-PAGE western blot of isolated mitochondria showed reduced levels of CIV in siCOX20-1 and siCOX20-2 relative to siCtrl. Complex II (SDHA) is indicative of loading. Data are shown as means ±SD (n=3). **p<0.01; n.s. = not significant. (G) BN-PAGE followed by in-gel activity assay showed reduced CIV activity demonstrated by reduced band density in siCOX20-1 and siCOX20-2 relative to siCtrl. (H) CIV substrates-driven oxygen consumption rates were measured on 50µg freshly isolated mitochondria in the high-resolution respirometry. Data are shown as means ±SD (n=3). *p<0.05. (I) Analysis of oxygen consumption using different inhibitors. The rates of oxygen consumption (OCR) were measured on 2 million cells of each cell group under basal conditions and then with sequential additions of oligomycin (proton leak), FCCP (maximal respiration), antimycin A/rotenone (non-mitochondrial oxygen) at the indicated times. (J) Statistical analysis was done for basal OCR, ATP-linked OCR, proton leak OCR, maximal OCR, reserve capacity OCR and non-mitochondrial OCR. Data are shown as means ±SD (n=3). *p<0.05; **p<0.01; ***p<0.001; n.s. = not significant. (K) TMRM staining was used to measure mitochondrial membrane potential. Scale bar, 100 µm. (L) Statistical analysis of TMRM

fluorescence intensity showed a significant reduction of mitochondrial membrane potential in siCOX20-1 and siCOX20-2 relative to siCtrl. Data are shown as means ±SD (n=3). ****p<0.0001. (M) Growth rate of ND7/23 cells in culture medium with glucose (25mM) or galactose (10mM). Growth rate was determined by the ratio of absorbance with specified medium for 4 days to absorbance seeded initially. Data are shown as means ±SD (n=3). **p<0.01; ***p<0.001. (N) Cell viability of ND7/23 cells in culture medium with hydrogen peroxide (200μM) for one hour. Data are shown as means ±SD (n=3). *p<0.05; n.s. = not significant.

Figure 6. Complex IV assembly, enzymatic activity and oxygen consumption rate in patients' fibroblasts. (A and B) BN-PAGE immunoblotting of respiratory chain complexes I–V from patient 1 and patient 5. (C) BN-PAGE showed reduced levels of CIV in fibroblasts of patient 1 compared to the control. Complex II (SDHA) is indicative of loading. Data are shown as means ± SD (n=3). *p<0.05; n.s. = not significant. (D) BN-PAGE showed reduced levels of CIV and complex V in fibroblasts of patient 5 compared to the control. Complex II (SDHA) is indicative of loading. Data are shown as means ± SD (n=3). *p<0.05; n.s. = not significant. (E) Mitochondrial respiratory chain complex IV enzymatic activity in fibroblasts. Data are shown as means ± SD (n=7). ****p<0.0001. (F) The rates of oxygen consumption (OCR) were measured on two million fibroblasts of each cell group under basal conditions and then with sequential additions of oligomycin (proton leak), FCCP (maximal respiration), antimycin A/rotenone (non-mitochondrial oxygen) at the indicated times. (G) Statistical analysis was done for basal OCR, ATP-linked OCR, maximal OCR, and reserve capacity OCR. Data are shown as means ± SD (n=3). *p<0.05; n.s. = not significant.

Table 1 Electrophysiological features of eight index patients

Patient (age at examination, years)	1 (38)		2 (33)		3 (29)		4 (13)		5 (25)		6 (4)		7 (15)		8 (7)		
Side	L	R	L	R	L	R	L	R	L	R	L	R	L	R	L	R	Normal value
Motor conduction																	
Median CMAP, mV	NA	14.5	20.5	13.2	15.6	13.6	10.7	9.0	18.2	14.0	NA	12.2	NA	12.1	10.0	12.4	>9.4
Median MCV, m/s	NA	56.1	57.3	52.1	51.6	50.8	51.5	47.8	46.7	46.2	NA	50.8	NA	61.0	47.0	46.3	>51.9
Ulnar CMAP, mV	NA	10.2	15.9	19.1	10.1	8.4	7.1	3.7	16.7	16.6	NA	12.6	NA	12.0	8.8	10.4	>7.0
Ulnar MCV, m/s	NA	59.2	68.1	68.7	56.9	53.8	48.4	51.4	52.6	39.0	NA	51.9	NA	59.4	49.1	52.7	>51.9
Peroneal CMAP, mV	3.9	6.8	5.1	4.0	3.4	3.3	0.99	0.46	5.3	7.8	NA	4.5	NA	4.6	3.4	4.9	>3.0
Peroneal MCV, m/s	38.9	43.5	45.2	43.7	42.4	40.6	33.7	NP	41.4	42.9	NA	45.9	NA	42.4	38.8	37.9	>45.1
Tibial CMAP, mV	13.2	14.3	20.3	19.2	22.0	23.9	7.8	7.6	25.0	18.8	NA	14.5	16.8	NA	13.7	15.6	>10.7
Tibial MCV, m/s	41.2	41.0	42.4	38.4	40.1	44.0	34.9	38.9	38.2	39.1	NA	49.6	40.3	NA	40.3	40.3	>42.1
Sensory conduction																	
Median SNAP, μV	NP	2.7	0.76	0.81	NP	NP	2.9	3.6	NP	NP	NP	NP	NA	NP	2.7	4.6	>12.3
Median SCV, m/s	NP	42.1	59.6	53.5	NP	NP	36.7	37.4	NP	NP	NP	NP	NA	NP	34.6	46.8	>53.1
Ulnar SNAP, μV	NP	NP	0.37	0.95	NP	NP	0.77	2.7	NP	NP	1.2	NP	NA	NP	8.3	2.7	>7.7
Ulnar SCV, m/s	NP	NP	46.0	53.1	NP	NP	24.1	40.9	NP	NP	45.7	NP	NA	NP	23.1	25.0	>51.8
Radial SNAP, μV	NP	NP	NA	NA	NP	NP	NA	NA	NP	NP	NA	NA	NA	NA	NA	NA	>10.7
Radial SCV, m/s	NP	NP	NA	NA	NP	NP	NA	NA	NP	NP	NA	NA	NA	NA	NA	NA	>45.1
Sural SNAP, μV	NP	NP	6.70	3.70	NP	NP	NP	NP	2.1	NA	NP	NP	NP	NA	8.1	2.4	>10.5
Sural SCV, m/s	NP	NP	25.1	31.3	NP	NP	NP	NP	40.4	NA	NP	NP	NP	NA	20.0	37.9	>46.6
Superficial peroneal SNAP, μV	NP	NP	5.4	3.0	NP	NP	NP	NP	3.8	5.4	NP	1.7	NP	NP	7.3	2.5	>7.6
Superficial peroneal SCV, m/s	NP	NP	23.1	25.1	NP	NP	NP	NP	38.2	25.9	NP	35.3	NP	NP	22.7	30.0	>39.8

L/R = left/right; MCV = motor nerve conduction velocity; SCV = sensory nerve conduction velocity; CMAP = compound muscle action potential; SNAP = sensory nerve action potential; NP = no potentials; NA = not available.

Table 2 Clinical manifestations of the eight index patients

Family	1	2	3	4	5	6	7	8
Mutation	p.K14R/p.K14R	p.K14R/p.K14R	p.K14R/p.K14R	p.K14R/p.W74C	p.K14R/p.W74C	p.K14R/p.S33L	p.K14R/c.157+7A>G	p.K14R/p.Q87*
Sex/age, years	Female/38	Female/35	Male/30	Male/15	Female/25	Female/5	Male/28	Male/11
AAO, years	17	5	15	5	14	1	7	1.5
Initial symptom	Difficulty walking	Difficulty walking	Difficulty walking	Difficulty walking	Difficulty walking	Difficulty walking	Difficulty walking	Difficulty walking
Foot deformity	Bilateral	Bilateral	Bilateral	Bilateral	Bilateral	-	Bilateral	Bilateral
FDS score	3	3	3	6	3	1	5	3
CMTNS score	12	6	7	21	6	5	11	9
Sensory system								
Pinprick sensation deficit	−	−	−	−	−	−	−	−
Vibration/joint position deficit	+/+	+/+	+/+	+/+	+/+	+/+	+/+	+/+
Romberg sign	+	+	+	+	+	+	+	+
Autonomic dysfunction	−	−	−	−	−	−	−	−
Painless ulceration	−	−	−	−	−	−	−	−
Pyramidal and peripheral motor system								
Limb weakness DUL/DLL	4/2	5/5	4/3	5/4	5/5	5/5	5/4	5/4
Muscle atrophy DUL/DLL	+/+	−/−	−/−	−/+	−/−	−/−	−/−	−/−
Absent or decreased DTRs	+	+	+	+	+	+	+	+
Babinski sign	−	−	−	−	−	−	−	−
Spinocerebellar system								
Oculomotor disturbance	−	−	−	−	−	−	−	−
Dysarthria	−	−	−	Mild	−	−	−	Mild
Cerebellar ataxia	−	−	−	−	−	−	−	−
Cognitive deficits	−	−	−	Mild	−	−	−	−
MRI								
Cerebral atrophy	−	−	−	+	−	−	−	−
Spinal cord atrophy	NA	+	NA	+	+	NA	NA	NA

AAO = age at onset; CMTNS = Charcot-Marie-Tooth Neuropathy Score; DTR = deep tendon reflex; DUL/DLL = distal upper limbs/ distal lower limbs; FDS = Functional Disability Scale; NA = not available.

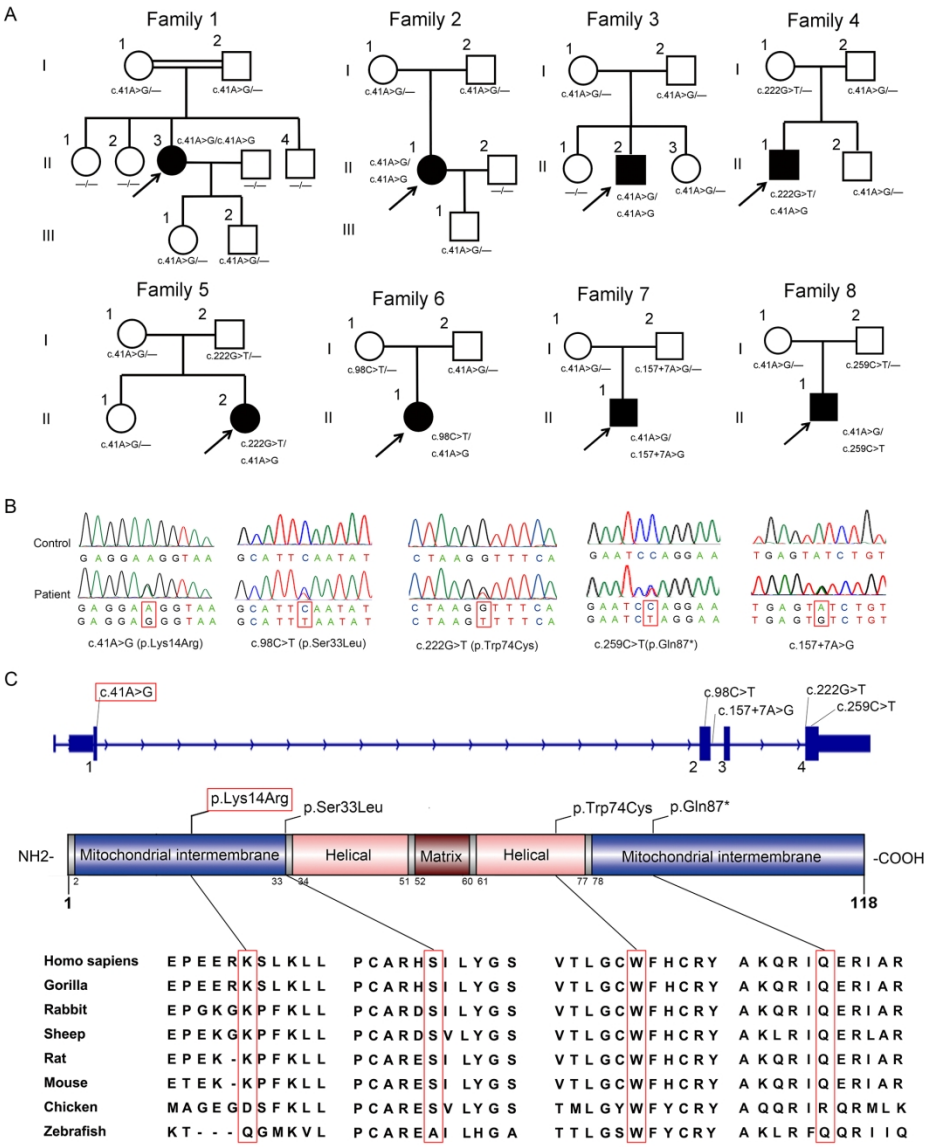

Bi-allelic variants in COX20 in eight unrelated autosomal recessive sensory neuronopathy families.

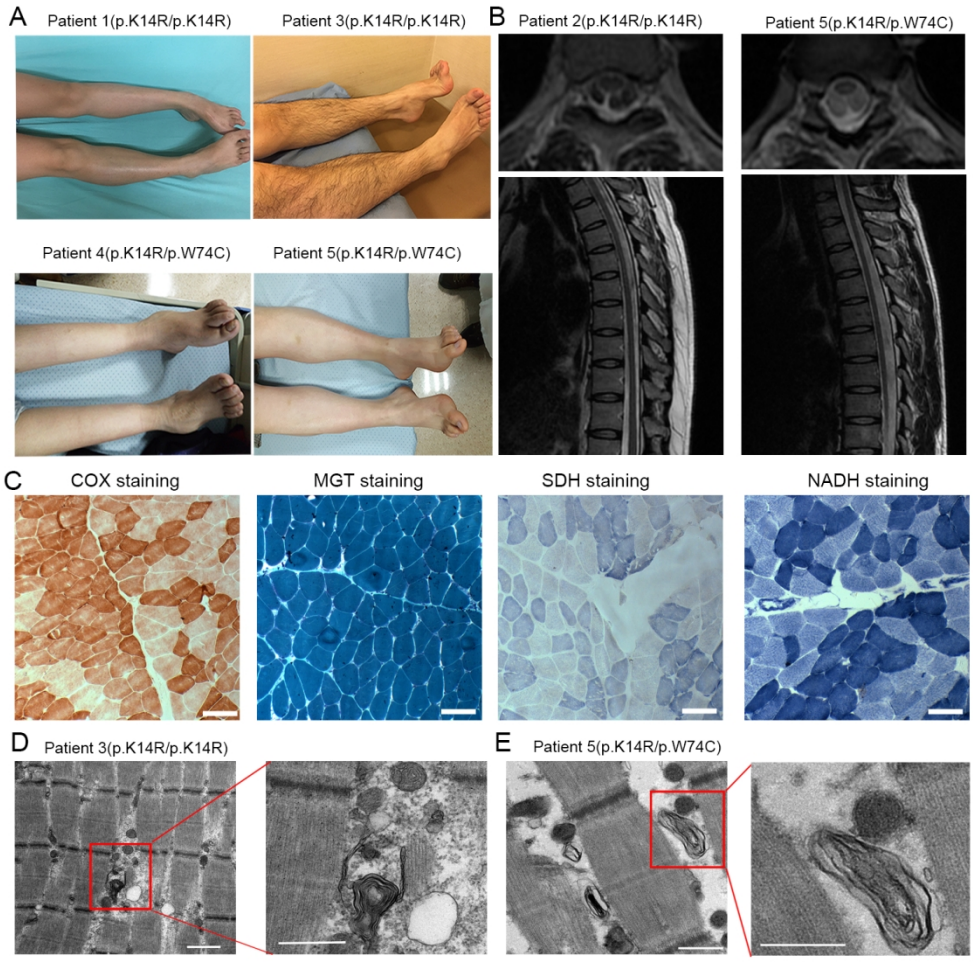

Clinical and histopathological features in patients.

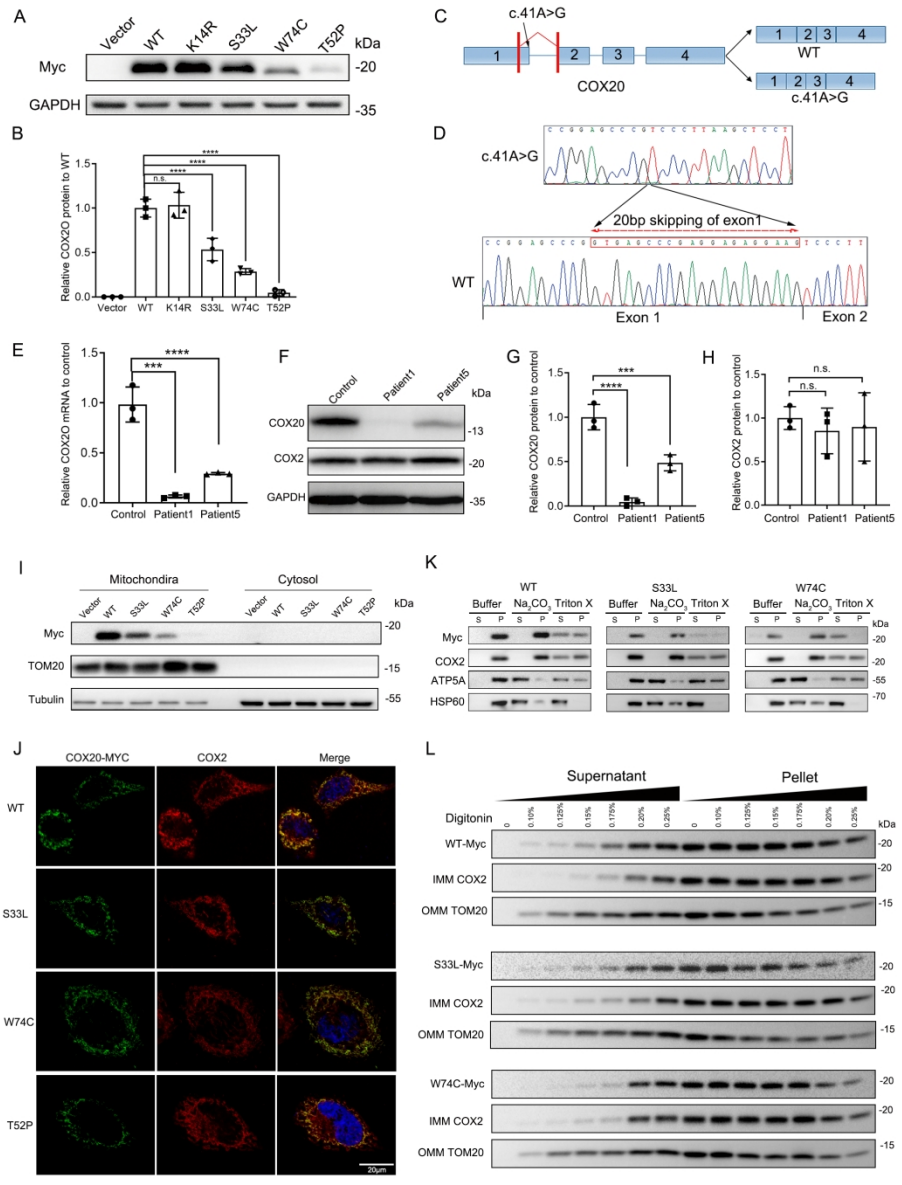

COX20 variants disrupt the expression level.

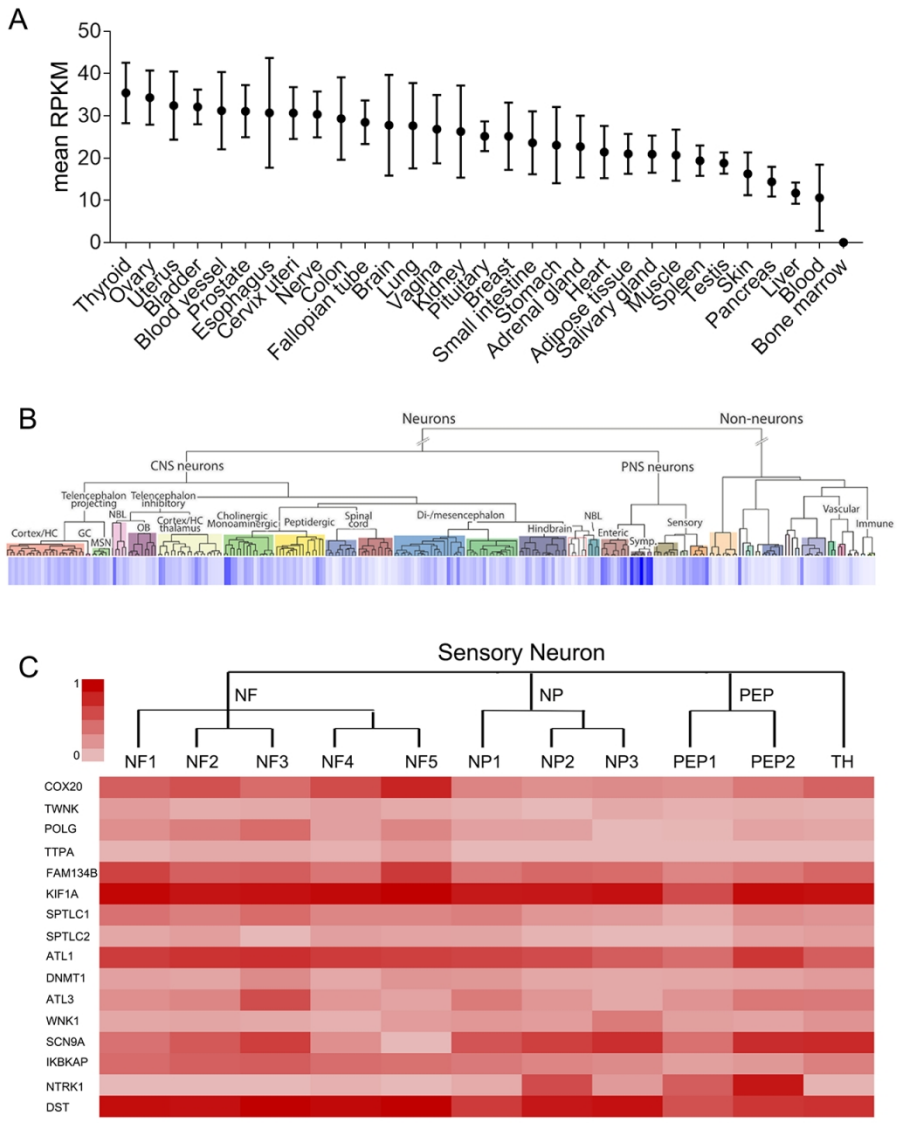

Expression of COX20 in tissues and cell types.

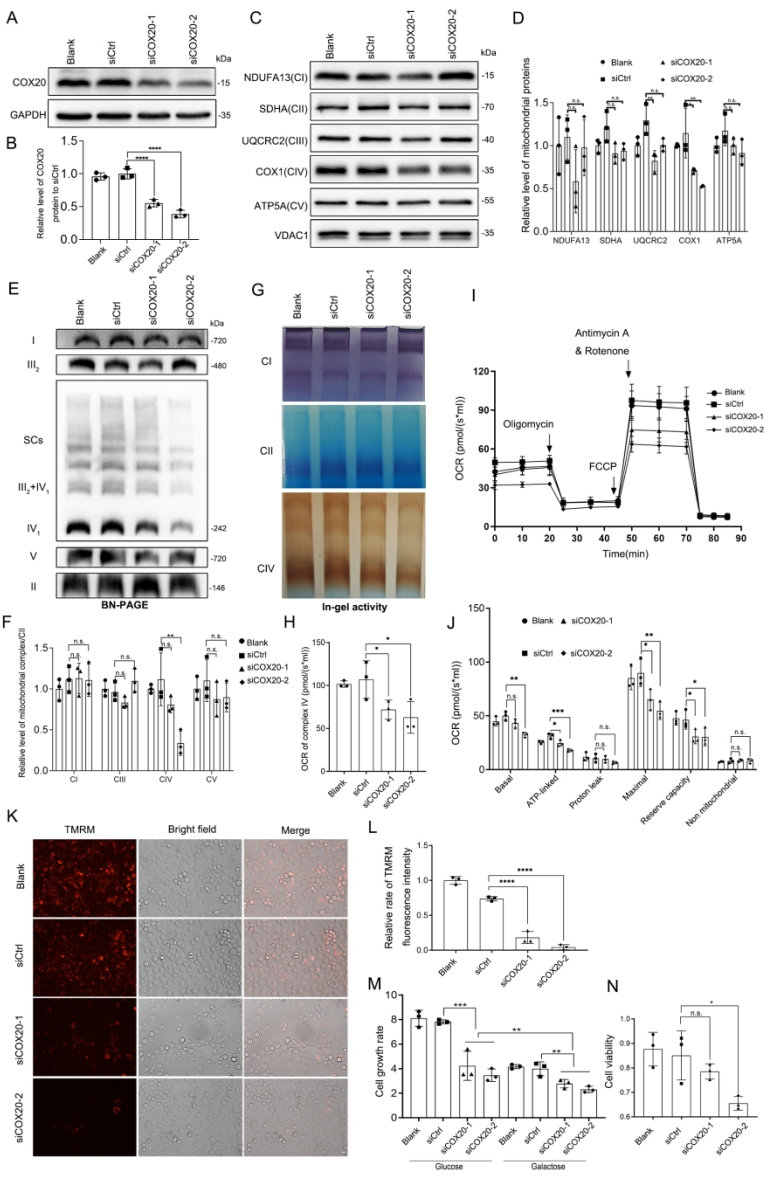

COX20 deficiency impairs COX assembly, enzymatic activity and mitochondrial bioenergetics in knockdown cells.

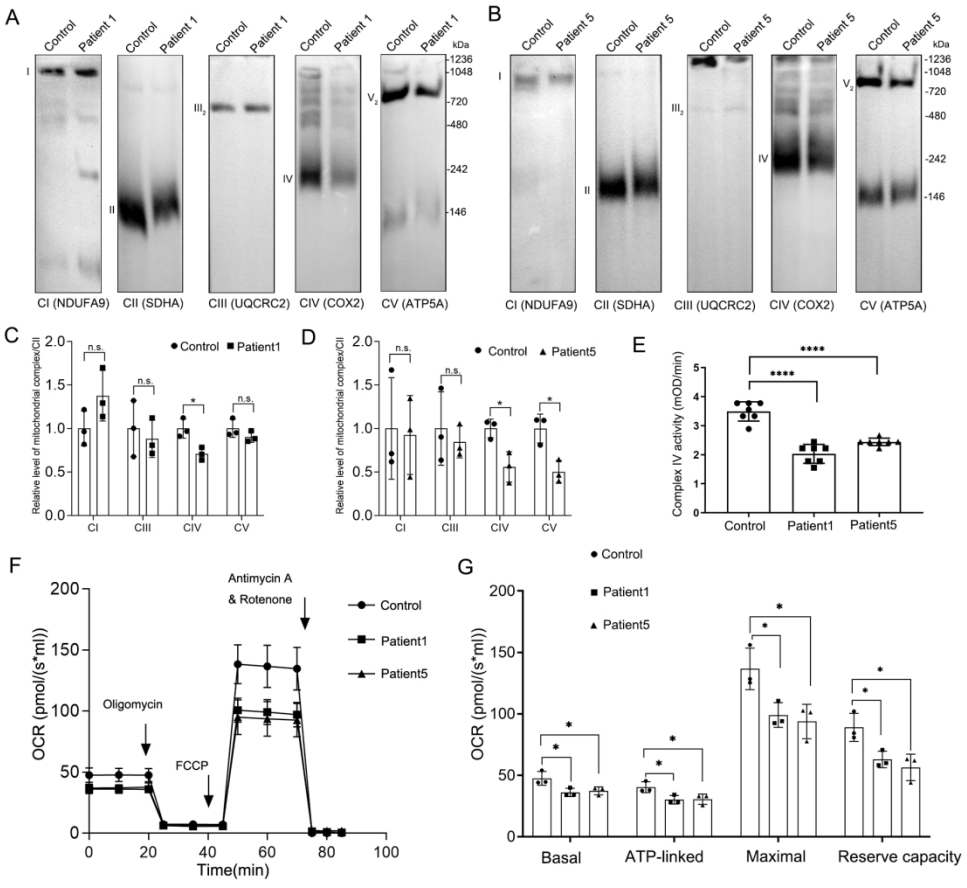

Complex IV assembly, enzymatic activity and oxygen consumption rate in patients' fibroblasts.